

Extremely strong spin-orbit coupling effect in light-element altermagnetic materials

Shuai Qu^{1,3}, Zhen-Feng Ouyang^{1,3}, Ze-Feng Gao^{1,2,3}, Hao Sun²,
Kai Liu^{1,3}, Peng-Jie Guo^{1,3*}, Zhong-Yi Lu^{1,3*}

¹ School of Physics and Beijing Key Laboratory of Opto-electronic Functional Materials & Micro-nano Devices. Renmin University of China, Beijing, 100872, China.

² Gaoling School of Artificial Intelligence, Renmin University of China, Beijing, China.

³ Key Laboratory of Quantum State Construction and Manipulation (Ministry of Education), Renmin University of China, Beijing, 100872, China.

*Corresponding author(s). E-mail(s): guopengjie@ruc.edu.cn;
zlu@ruc.edu.cn;

Abstract

Spin-orbit coupling is a key to realize many novel physical effects in condensed matter physics. Altermagnetic materials possess the duality of real-space antiferromagnetism and reciprocal-space ferromagnetism. It has not been explored that achieving strong spin-orbit coupling effect in light-element altermagnetic materials. In this work, based on symmetry analysis, the first-principles electronic structure calculations plus Dynamical Mean Field Theory, we demonstrate that there is strong spin-orbit coupling effect in light-element altermagnetic materials **NiF₃** and **FeCO₃**, and then propose a mechanism for realizing such effective spin-orbit coupling. This mechanism reveals the cooperative effect of crystal symmetry, electron occupation, electronegativity, electron correlation, and intrinsic spin-orbit coupling. Our work provides an approach for searching light-element altermagnetic materials with an effective strong spin-orbit coupling.

1 Introduction

Spin-orbit coupling (SOC) is ubiquitous in realistic materials and crucial for many novel physical phenomena emerging in condensed matter physics, including topological physics [1–3], anomalous Hall effect [4], spin Hall effect [5, 6], magnetocrystalline anisotropy [7] and so on. For instance, quantum anomalous Hall (QAH) insulators are characterized by non-zero Chern numbers [8]. The Chern number is derived from the integration of Berry curvature over the occupied state of the Brillouin zone (BZ). For collinear ferromagnetic and antiferromagnetic systems, the integral of Berry curvature over the occupied state in the Brillouin zone must be zero without SOC due to the spin symmetry $\{C_2^\perp T | T\}$. Here the C_2^\perp and T represent the 180 degrees rotation perpendicular to the spin direction and time-reversal operation, respectively. Therefore, QAH effect can only be realized in collinear magnetic systems when SOC is included [9, 10]. On the other hand, strong SOC may open up a large nontrivial bandgap, which is very important to realize QAH effect at high temperatures. In general, strong SOC exists in heavy-element compounds. Unfortunately, the chemical bonds of heavy element compounds are weaker than those of light-element compounds, which leads to more defects in heavy-element compounds. Thus, the stability to realize exotic functionalities in heavy element compounds is relatively weak.

An interesting question is whether the strong SOC effect can be achieved in light-element compounds. In 2008, Liu et al. proposed the correlation-enhanced spin-orbit effect in paramagnetic Sr_2RhO_4 [11]. Very recently, Li et al. demonstrated that the SOC can be enhanced in light-element ferromagnetic materials, which derives from the cooperative effect of crystal symmetry, electron occupancy, electron correlation, and intrinsic SOC [12]. This provides a new direction for the design of light-element materials with strong effective SOC.

Very recently, altermagnetism is proposed as a new magnetic phase possessing the duality of real-space antiferromagnetism and reciprocal-space ferromagnetism, distinct from ferromagnetism and conventional collinear antiferromagnetism [13, 14]. Moreover, altermagnetic materials have a wide range of electronic properties, which cover metals, semi-metals, semiconductors, and insulators [14, 15]. Different from ferromagnetic materials with s -wave spin polarization, altermagnetic materials have \mathbf{k} -dependent spin polarization, which results in many exotic physical effects [13, 14, 16–23]. With SOC, similar to the case of ferromagnetic materials, the time-reversal symmetry-breaking macroscopic phenomena can be also realized in altermagnetic materials [10, 24–26]. Nevertheless, altermagnetism is proposed based on spin group theory [27–30] and the predicted altermagnetic materials have many light-element compounds [14, 15, 28]. Therefore, it is very important to propose a mechanism to enhance SOC in light-element compounds with altermagnetism and predict the corresponding compounds with strong SOC effect.

In this work, based on symmetry analysis, the first-principles electronic structure calculations based on density functional theory (DFT) plus Dynamical Mean Field Theory (DMFT), we predict that the light-element compounds NiF_3 and FeCO_3 are i -wave altermagnetic materials with extremely strong SOC effect. Then, we further propose a mechanism to enhance SOC effect in light-element compounds with altermagnetism, which reveals the cooperative effect of crystal symmetry, electron

occupation, electronegativity, electron correlation, and intrinsic SOC. We also explain the weak SOC effect in alternating materials VF_3 , CrF_3 , FeF_3 and CoF_3 .

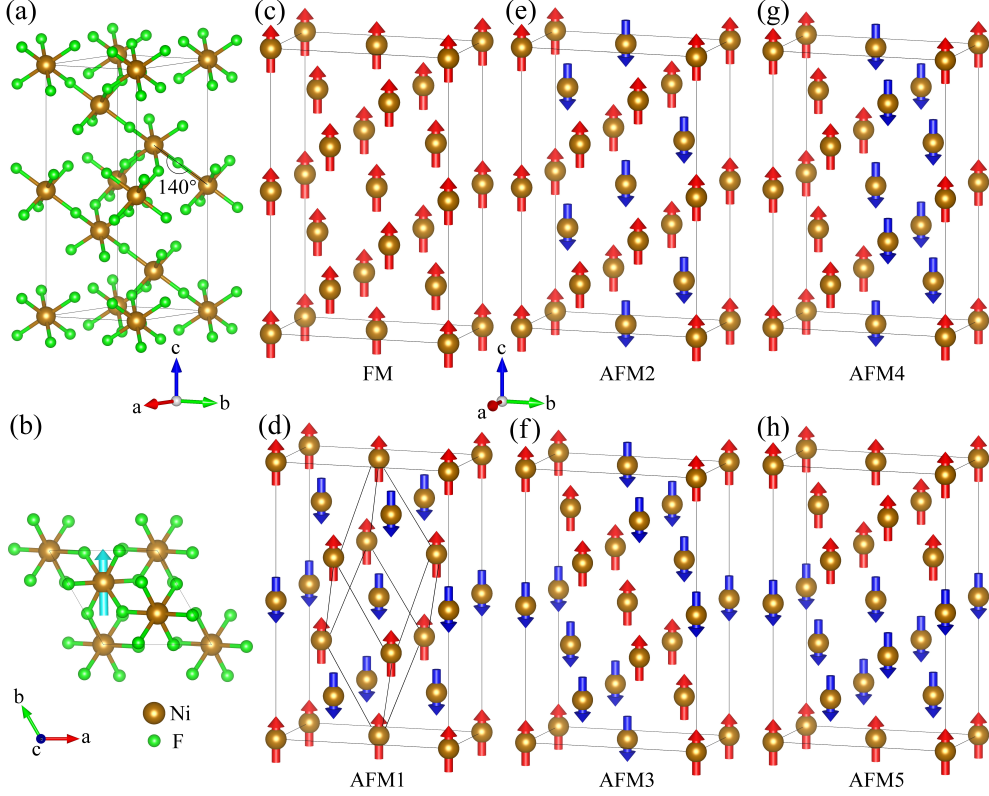


Fig. 1 The crystal structure and six collinear magnetic structures of NiF_3 . (a) and (b) are side and top views of the crystal structure, respectively. The cyan arrow represents the direction of easy magnetization axis. (c)-(h) are six different collinear magnetic structures including one ferromagnetic and five different collinear antiferromagnetic structures. The bond angle of Ni-F-Ni for the nearest neighbor Ni ions is 140 degrees. The primitive cell of NiF_3 is shown in (d). The red and blue arrows represent spin-up and spin-down magnetic moments, respectively.

2 Results

The NiF_3 takes rhombohedral structure with nonsymmorphic $R\bar{3}c$ (167) space group symmetry (Fig.1(a) and (b)). The corresponding elementary symmetry operations are C_{3z} , C_2^t and I , which yield the point group D_{3d} . The t represents $(1/2, 1/2, 1/2)$ fractional translation. To confirm the magnetic ground state of NiF_3 , we consider six different magnetic structures, including one ferromagnetic and five collinear antiferromagnetic structures which are shown in Fig.1(c)-(h). Then we calculate relative energies of six magnetic states with the variation of correlation interaction U . With the

increase of correlation interaction U , the NiF_3 changes from the ferromagnetic state to AFM1 state (Fig.2(a)). The AFM1 is of intralayer ferromagnetism and interlayer antiferromagnetism (Fig.1(d)), namely so-called G-type antiferromagnetic order in literature. In previous works, the correlation interaction U was selected as 6.7 eV for Ni $3d$ orbitals [31, 32]. Thus, the magnetic ground state of NiF_3 is the AFM1 state, which is consistent with previous works [15]. On the other hand, since the bond angle of Ni-F-Ni for the nearest neighbor Ni ions is 140 degrees, the spins of the nearest neighbor and next nearest neighbor Ni ions are in antiparallel and parallel arrangement according to Goodenough-Kanamori rules [33], respectively. This will result in NiF_3 being the collinear antiferromagnetic state AFM1. Thus, the results of theoretical analysis are in agreement with those of theoretical calculation.

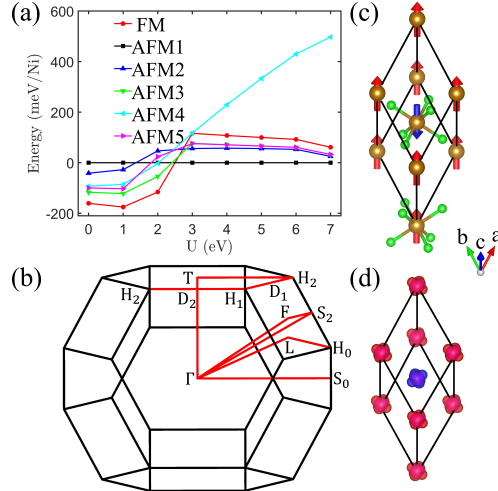


Fig. 2 The magnetic ground state of NiF_3 and the corresponding properties. (a) Relative energies of six different magnetic states with the variation of correlation interaction U . (b) and (c) are the corresponding Brillouin zone and the magnetic primitive cell of NiF_3 , respectively. The high-symmetry lines and points are marked in the BZ. The red and blue arrows represent spin-up and spin-down magnetic moments, respectively. (d) The anisotropic polarization charge densities. The red and blue represent spin-up and spin-down polarization charge density, respectively.

Indeed, the AFM1 state is very simple and the corresponding magnetic primitive cell only contains two magnetic atoms. From Fig.2(c), the two Ni atoms with opposite spin arrangement are surrounded by F-atom octahedrons with different orientations, respectively. Thus, the two opposite spin Ni sublattices cannot be connected by a fractional translation. Due to two Ni ions located at space-inversion invariant points, the two opposite spin Ni sublattices cannot be either connected by space-inversion symmetry. However, the two opposite spin Ni sublattices can be connected by C_2^+ symmetry. Thus, the NiF_3 is an altermagnetic material. The BZ of altermagnetic NiF_3 is shown in Fig.2(b) and both the high-symmetry lines and points are marked. In order to display the altermagnetic properties more intuitively, we calculate polarization charge density of altermagnetic NiF_3 . From Fig.2(d), the polarization charge densities of two

Ni ions with opposite spin arrangement are anisotropic and their orientations are different, deriving from F-atom octahedrons with different orientations. The anisotropic polarization charge densities can result in k -dependent spin polarization in reciprocal space. Moreover, according to different spin group symmetries, the k -dependent spin polarization can form d -wave, g -wave, or i -wave magnetism [13].

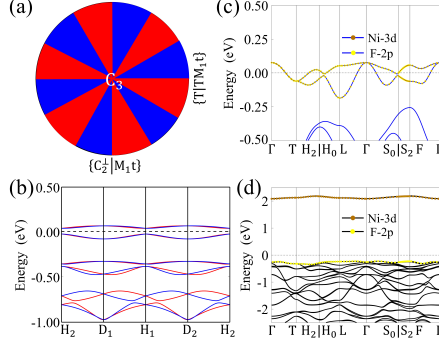


Fig. 3 Schematic diagram of the i -wave magnetism and electronic band structures of altermagnetic NiF_3 . (a) Schematic diagram of the i -wave magnetism. The red and blue parts represent spin up and down, respectively. (b) The electronic band structure without SOC along the high-symmetry directions. The red and blue lines represent spin-up and spin-down bands, respectively. (c) and (d) are the electronic band structures without and with SOC along the high-symmetry directions.

Without SOC, the nontrivial elementary spin symmetry operations in altermagnetic NiF_3 have $\{E||C_{3z}\}$, $\{C_2^\perp||M_1t\}$, $\{E||I\}$. The spin symmetries $\{C_2^\perp||M_1t\}$, $\{T||TM_1t\}$, and $\{E||C_{3z}\}$ make altermagnetic NiF_3 being an i -wave magnetic material, as shown in Fig. 3 (a). Meanwhile, the spins of bands are opposite along the $H_2 - D_1$ ($H_2 - D_2$) and $D_1 - H_2$ ($D_2 - H_1$) directions, reflecting features of i -wave magnetism (Fig.3(b)).

In order to well understand the electronic properties, we also calculate the electronic band structures of altermagnetic NiF_3 . Without SOC, the NiF_3 is an altermagnetic metal. There are four bands crossing the Fermi level due to spin degeneracy on the high-symmetry directions (Fig.3 (c)). Especially, these four bands are degenerate on the $\Gamma - T$ axis. In fact, any k point on the $\Gamma - T$ axis has nontrivial elementary spin symmetry operations $\{E||C_{3z}\}$ and $\{C_2^\perp||M_1t\}$. And the spin symmetry $\{E||C_{3z}\}$ has one one-dimensional irreducible real representation and two one-dimensional irreducible complex representations. Although the time-reversal symmetry is broken, altermagnetic materials can have equivalent time-reversal spin symmetry $\{C_2^\perp T||IT\}$. The spin symmetry $\{C_2^\perp T||IT\}$ will result in two one-dimensional irreducible complex representations to form a Kramers degeneracy. Meanwhile, the spin symmetry $\{C_2^\perp||M_1t\}$ protects the spin degeneracy. Therefore, there is one four-dimensional and one two-dimensional irreducible representations on the $\Gamma - T$ axis. The quadruple degenerate band crossing the Fermi level is thus protected by the spin group symmetry. Furthermore, the orbital weight analysis shows that these four bands are contributed by both the $3d$ orbitals of Ni and the p orbitals of F (Fig.3 (c)). As is known to all, the F atom has the strongest electronegativity among all chemical elements, but

the $2p$ orbitals of F do not fully acquire the $3d$ -orbital electrons of Ni, which is very interesting.

In our calculations, the number of valence electrons of NiF_3 is 74, which makes the quadruple band only half-filled. This is the reason why the p orbitals of F do not fully acquire the d -orbital electrons of Ni. When SOC is included, the spin group symmetry breaks down to magnetic group symmetry. The reduction of symmetry will result in the quadruple band to split into four non-degenerate bands. Since the F atom has the strongest electronegativity, the $2p$ orbitals of F will completely acquire the $3d$ -orbital electrons of Ni. This will result in altermagnetic NiF_3 to transform from metal phase to insulator phase. In order to prove our theoretical analysis, we calculate the electronic band structure of altermagnetic NiF_3 with SOC. Just like our theoretical analysis, the $2p$ orbitals of F indeed fully acquire the $3d$ -orbital electrons of Ni and altermagnetic NiF_3 transforms into an insulator with a bandgap of 2.31 eV (Fig.3 (d)). In general, the SOC strength of Ni is in the order of 10 meV, so the effective SOC strength of altermagnetic NiF_3 is two orders of magnitude higher than that of Ni. Thus, the SOC effect of altermagnetic NiF_3 is extremely strong.

In order to examine the effect of correlation interaction, we also calculate the electronic band structures of altermagnetic NiF_3 under correlation interaction $U = 3, 5, 7\text{eV}$, which are shown in Fig.4 (a), (b), and (c), respectively. From Fig.4 (a), (b) and (c), the correlation interaction has a slight effect on the band structure around the Fermi level without SOC, due to the constraints of spin symmetry and electron occupancy being 74. When including SOC, altermagnetic NiF_3 transforms from a metal phase to an insulator phase under different correlation interaction U . Moreover, the bandgap of altermagnetic NiF_3 increases linearly with the correlation interaction U (Fig.4 (d)). Thus, the correlation interaction can substantially enhance the bandgap opened by the SOC of altermagnetic materials. In order to make our results more reliable, we have also further completed the calculations respectively with hybrid functional and DFT+DMFT but without SOC. All these calculations are consistent with the calculated results of GGA+U, which are shown in Supplementary Material (SM).

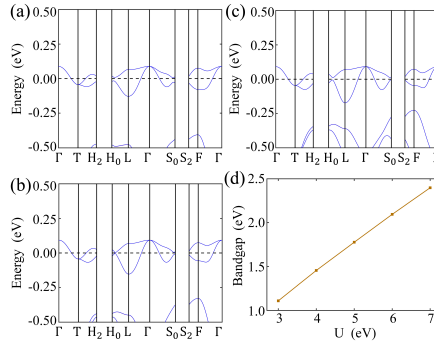


Fig. 4 The electronic properties of altermagnetic NiF_3 under different correlation interaction U . (a), (b) and (c) are the electronic band structures along the high-symmetry directions without SOC under correlation interaction $U = 3, 5, 7\text{eV}$, respectively. (d) The bandgap as a function of correlation interaction U under SOC.

3 Discussion

Now we well understand the reason for the extremely strong SOC effect in altermagnetic NiF_3 . A natural question is whether such a strong SOC effect can be realized in other altermagnetic materials. According to the above analysis, we propose four conditions for realizing such an effective strong SOC in light-element altermagnetic materials: First, the spin group of altermagnetic material has high-dimensional (greater than four dimensions) irreducible representation (crystal symmetry groups are presented in the SM [34]); Second, the band with high-dimensional representation crossing the Fermi level is half-filled by valence electrons; Third, non-metallic elements have strong electronegativity; Fourth, the altermagnetic material has strong electron correlation. To verify these four conditions, we further calculate the electronic band structures of four *i*-wave altermagnetic materials (VF_3 , CrF_3 , FeF_3 , CoF_3 , and FeCO_3), which have the same crystal structure and magnetic structure as NiF_3 [15]. Our calculations show that these four materials (VF_3 , CrF_3 , FeF_3 , and CoF_3) do not satisfy the second condition, while FeCO_3 satisfies all four conditions. Therefore, the SOC effect of these four materials is weak (Fig. A2), but the SOC effect of FeCO_3 is extremely strong (Fig. A3). On the other hand, since high-dimensional irreducible representations can be protected by spin space group in two-dimensional altermagnetic systems, the proposed mechanism is also applicable to two-dimensional light element altermagnetic materials, which may be advantage for realizing quantum anomalous Hall effect at high temperatures [10].

The mechanism for enhancing the SOC effect that we propose in altermagnetic materials is different from that in ferromagnetic materials [12]. First, the high-dimensional representation of the symmetry group is 2 or 3 dimensions in ferromagnetism, while in altermagnetism the high-dimension representation is 4 or 6 dimensions, so their symmetry requirements are entirely different. Second, the band with high-dimensional representation in ferromagnetism comes from *d* orbitals, while the band with high-dimensional representation in altermagnetism can come from the combination of *p* orbitals and *d* orbitals. Third, the enhancement of SOC effect derives from correlation interaction for ferromagnetic materials, but from both correlation interaction and the electronegativity of nonmetallic element for altermagnetic materials. Due to one more degree of freedom to enhance the SOC effect, a stronger SOC effect can be achieved in the altermagnetic materials. Moreover, if the electronegativity of nonmetallic element is weak, different topological phases may be realized in altermagnetic materials when including SOC. On the other hand, the mechanism for enhancing SOC effect in altermagnetic materials can be also generalized to conventional antiferromagnetic materials. Due to the equivalent time-reversal symmetry, more spin groups with conventional antiferromagnetism have high-dimensional irreducible representations. Moreover, conventional antiferromagnetic materials are more abundant than altermagnetic materials, thus conventional light-element antiferromagnetic materials with strong SOC effect remain to be discovered.

In experiment, a recent experiment suggests that NiF_3 is a semiconductor [35], which is consistent with our calculations. This provides a strong evidence that NiF_3 has a strong SOC effect. Different from NiF_3 , FeCO_3 has not only been synthesized experimentally [36], but also its magnetic structure has been confirmed by neutron

scattering experiments [37]. Therefore, FeCO_3 must have strong SOC effect, which can be confirmed by the APPES experiment and the first-principles electronic structure calculations. Finally, the metal phase of NiF_3 is unstable, and both the Jahn-Teller and SOC effects can transform NiF_3 into a stable insulator phase. Our calculations show that the SOC effect dominates the electronic properties of NiF_3 rather than the Jahn-Teller effect (Detailed calculations and analysis are presented in the SM [34]).

4 Conclusion

Based on symmetry analysis and the first-principles electronic structure calculations, we demonstrate that there is extremely strong SOC effect in altermagnetic materials NiF_3 and FeCO_3 . Then, we propose a mechanism to enhance SOC effect in altermagnetic materials. This mechanism reveals the cooperative effect of crystal symmetry, electron occupation, electronegativity, electron correlation, and intrinsic spin-orbit coupling. The mechanism can explain not only the strong SOC effect in altermagnetic NiF_3 , but also the weak SOC in altermagnetic VF_3 , CrF_3 , FeF_3 , CoF_3 . Moreover, the mechanism for enhancing SOC effect can be also generalized to two-dimensional altermagnetic materials, being beneficial to realize quantum anomalous Hall effect at high temperatures.

5 Methods

The first-principles electronic structure calculations were performed within the framework of density functional theory (DFT) [38, 39] using the Vienna ab initio Simulation Package (VASP) [40–42] and Quantum ESPRESSO [43]. The generalized gradient approximation (GGA) of the Perdew-Burke-Ernzerhof (PBE) type [44] and the meta-GGA of the Strongly Constrained and Appropriately Normed (SCAN) type [45] were employed for the exchange-correlation functionals. The projector augmented wave (PAW) method [46, 47] was adopted to describe the interactions between valence electrons and nuclei. The kinetic-energy cutoff for the plane-wave basis was set to 600 eV. Total energy convergence and atomic force tolerance were established at 10^{-6} eV and 10^{-4} eV/Å, respectively. To describe the Fermi-Dirac distribution function, a Gaussian smearing of 0.05 eV was used. The $16 \times 16 \times 16$ and $8 \times 8 \times 4$ Monkhorst-Pack k meshes were employed for BZ sampling of the unit cell and supercell, respectively. To account for the correlation effects of Ni $3d$ orbitals, we performed GGA+U [48] calculations by using the rotationally invariant approach introduced by Liechtenstein et al [49] and the simplified rotationally invariant version of Dudarev et al [50]. The empirical Hubbard U parameter for Ni $3d$ orbitals was determined to be 6.7 eV according to previous studies [31, 32, 51].

The Heyd-Scuseria-Ernzerhof (HSE) functional [52] implemented in Quantum ESPRESSO significantly enhanced the accuracy of electronic band structure calculations of altermagnetic NiF_3 without SOC by integrating both local and non-local exchange-correlation contributions. The gygi-baldereschi approach was used for treating the Coulomb potential divergencies at small sampling vectors of the Fock operator.

Momentum-resolved spectral function obtained by the DFT+DMFT (dynamical mean-field theory) calculations without SOC for altermagnetic NiF₃ at temperature $T = 200\text{K}$ by hybridization expansion continuous-time quantum impurity solver [53] based on the EDMFTF package [54]. And an “exact” double-counting scheme developed by Haule [55] was used. The real-frequency self-energy function was obtained by analytical continuation with the maximum entropy. Then it was used to calculate the momentum-resolved spectral function. And density-density form of the Coulomb repulsion was used. The $3d$ orbitals of Ni were considered to be correlated.

6 Data availability

Data are available from the corresponding authors (Peng-Jie Guo and Zhong-Yi Lu) upon reasonable request. We employed the density functional theory code VASP and EDMFTF, which can be obtained and purchased at <http://www.vasp.at> and <http://hauleweb.rutgers.edu/>, respectively.

References

- [1] Hasan, M.Z., Kane, C.L.: Colloquium: Topological insulators. *Rev. Mod. Phys.* **82**, 3045–3067 (2010) <https://doi.org/10.1103/RevModPhys.82.3045>
- [2] Qi, X.-L., Zhang, S.-C.: Topological insulators and superconductors. *Rev. Mod. Phys.* **83**, 1057–1110 (2011) <https://doi.org/10.1103/RevModPhys.83.1057>
- [3] Bansil, A., Lin, H., Das, T.: Colloquium: Topological band theory. *Rev. Mod. Phys.* **88**, 021004 (2016) <https://doi.org/10.1103/RevModPhys.88.021004>
- [4] Nagaosa, N., Sinova, J., Onoda, S., MacDonald, A.H., Ong, N.P.: Anomalous hall effect. *Rev. Mod. Phys.* **82**, 1539–1592 (2010) <https://doi.org/10.1103/RevModPhys.82.1539>
- [5] Sinova, J., Valenzuela, S.O., Wunderlich, J., Back, C.H., Jungwirth, T.: Spin hall effects. *Rev. Mod. Phys.* **87**, 1213–1260 (2015) <https://doi.org/10.1103/RevModPhys.87.1213>
- [6] Hirsch, J.E.: Spin hall effect. *Phys. Rev. Lett.* **83**, 1834–1837 (1999) <https://doi.org/10.1103/PhysRevLett.83.1834>
- [7] Cinal, M., Edwards, D.M., Mathon, J.: Magnetocrystalline anisotropy in ferromagnetic films. *Phys. Rev. B* **50**, 3754–3760 (1994) <https://doi.org/10.1103/PhysRevB.50.3754>
- [8] Haldane, F.D.M.: Model for a quantum hall effect without landau levels: Condensed-matter realization of the “parity anomaly”. *Phys. Rev. Lett.* **61**, 2015–2018 (1988) <https://doi.org/10.1103/PhysRevLett.61.2015>

- [9] Chang, C.-Z., Liu, C.-X., MacDonald, A.H.: Colloquium: Quantum anomalous hall effect. *Rev. Mod. Phys.* **95**, 011002 (2023) <https://doi.org/10.1103/RevModPhys.95.011002>
- [10] Guo, P.-J., Liu, Z.-X., Lu, Z.-Y.: Quantum anomalous hall effect in collinear antiferromagnetism. *npj Comput. Mater.* **9**(1), 70 (2023) <https://doi.org/10.1038/s41524-023-01025-4>
- [11] Liu, G.-Q., Antonov, V.N., Jepsen, O., Andersen, O.K.: Coulomb-enhanced spin-orbit splitting: The missing piece in the Sr_2RhO_4 puzzle. *Phys. Rev. Lett.* **101**, 026408 (2008) <https://doi.org/10.1103/PhysRevLett.101.026408>
- [12] Li, J.-Y., Yao, Q.-S., Wu, L., Hu, Z.-X., Gao, B.-Y., Wan, X.-G., Liu, Q.-H.: Designing light-element materials with large effective spin-orbit coupling. *Nat. Commun.* **13**(1), 919 (2022) <https://doi.org/10.1038/s41467-022-28534-y>
- [13] Šmejkal, L., Sinova, J., Jungwirth, T.: Beyond conventional ferromagnetism and antiferromagnetism: A phase with nonrelativistic spin and crystal rotation symmetry. *Phys. Rev. X* **12**, 031042 (2022) <https://doi.org/10.1103/PhysRevX.12.031042>
- [14] Šmejkal, L., Sinova, J., Jungwirth, T.: Emerging research landscape of altermagnetism. *Phys. Rev. X* **12**, 040501 (2022) <https://doi.org/10.1103/PhysRevX.12.040501>
- [15] Gao, Z.-F., Qu, S., Zeng, B., Liu, Y., Wen, J.-R., Sun, H., Guo, P.-J., Lu, Z.-Y.: Ai-accelerated discovery of altermagnetic materials. *National Science Review* **12**(4), 066 (2025) <https://doi.org/10.1093/nsr/nwaf066> <https://academic.oup.com/nsr/article-pdf/12/4/nwaf066/62054665/nwaf066.pdf>
- [16] Ma, H.-Y., Hu, M.-L., Li, N.-N., Liu, J.-P., Yao, W., Jia, J.-F., Liu, J.-W.: Multifunctional antiferromagnetic materials with giant piezomagnetism and non-collinear spin current. *Nat. Commun.* **12**(1), 2846 (2021) <https://doi.org/10.1038/s41467-021-23127-7>
- [17] Šmejkal, L., Hellenes, A.B., González-Hernández, R., Sinova, J., Jungwirth, T.: Giant and tunneling magnetoresistance in unconventional collinear antiferromagnets with nonrelativistic spin-momentum coupling. *Phys. Rev. X* **12**, 011028 (2022) <https://doi.org/10.1103/PhysRevX.12.011028>
- [18] González-Hernández, R., Šmejkal, L., Výborný, K., Yahagi, Y., Sinova, J., Jungwirth, T., Železný, J.: Efficient electrical spin splitter based on nonrelativistic collinear antiferromagnetism. *Phys. Rev. Lett.* **126**, 127701 (2021) <https://doi.org/10.1103/PhysRevLett.126.127701>
- [19] Bai, H., Han, L., Feng, X.Y., Zhou, Y.J., Su, R.X., Wang, Q., Liao, L.Y., Zhu,

- W.X., Chen, X.Z., Pan, F., Fan, X.L., Song, C.: Observation of spin splitting torque in a collinear antiferromagnet RuO₂. Phys. Rev. Lett. **128**, 197202 (2022) <https://doi.org/10.1103/PhysRevLett.128.197202>
- [20] Karube, S., Tanaka, T., Sugawara, D., Kadoguchi, N., Kohda, M., Nitta, J.: Observation of spin-splitter torque in collinear antiferromagnetic RuO₂. Phys. Rev. Lett. **129**, 137201 (2022) <https://doi.org/10.1103/PhysRevLett.129.137201>
- [21] Zhu, D., Zhuang, Z.-Y., Wu, Z.-G., Yan, Z.-B.: Topological superconductivity in two-dimensional altermagnetic metals. Phys. Rev. B **108**, 184505 (2023) <https://doi.org/10.1103/PhysRevB.108.184505>
- [22] Guo, P.-J., Gu, Y.-H., Gao, Z.-F., Lu, Z.-Y.: Altermagnetic ferroelectric LiFe₂F₆ and spin-triplet excitonic insulator phase (2023)
- [23] Zhou, X.-D., Feng, W.-X., Zhang, R.-W., Šmejkal, L., Sinova, J., Mokrousov, Y., Yao, Y.-G.: Crystal thermal transport in altermagnetic RuO₂. Phys. Rev. Lett. **132**, 056701 (2024) <https://doi.org/10.1103/PhysRevLett.132.056701>
- [24] Šmejkal, L., González-Hernández, R., Jungwirth, T., Sinova, J.: Crystal time-reversal symmetry breaking and spontaneous hall effect in collinear antiferromagnets. Sci. Adv. **6**(23), 8809 (2020) <https://doi.org/10.1126/sciadv.aaz8809>
- [25] Zhou, X.-D., Feng, W.-X., Yang, X.-X., Guo, G.-Y., Yao, Y.-G.: Crystal chirality magneto-optical effects in collinear antiferromagnets. Phys. Rev. B **104**, 024401 (2021) <https://doi.org/10.1103/PhysRevB.104.024401>
- [26] Hou, X.-Y., Yang, H.-C., Liu, Z.-X., Guo, P.-J., Lu, Z.-Y.: Large intrinsic anomalous hall effect in both Nb₂FeB₂ and Ta₂FeB₂ with collinear antiferromagnetism. Phys. Rev. B **107**, 161109 (2023) <https://doi.org/10.1103/PhysRevB.107.161109>
- [27] Guo, P.-J., Wei, Y.-W., Liu, K., Liu, Z.-X., Lu, Z.-Y.: Eightfold degenerate fermions in two dimensions. Phys. Rev. Lett. **127**, 176401 (2021) <https://doi.org/10.1103/PhysRevLett.127.176401>
- [28] Xiao, Z.-Y., Zhao, J.-Z., Li, Y.-Q., Shindou, R., Song, Z.-D.: Spin space groups: Full classification and applications. Phys. Rev. X **14**, 031037 (2024) <https://doi.org/10.1103/PhysRevX.14.031037>
- [29] Jiang, Y., Song, Z.-Y., Zhu, T.-N., Fang, Z., Weng, H.-M., Liu, Z.-X., Yang, J., Fang, C.: Enumeration of spin-space groups: Toward a complete description of symmetries of magnetic orders. Phys. Rev. X **14**, 031039 (2024) <https://doi.org/10.1103/PhysRevX.14.031039>
- [30] Chen, X., Liu, Y., Liu, P., Yu, Y., Ren, J., Li, J., Zhang, A., Liu, Q.: Unconventional magnons in collinear magnets dictated by spin space groups. Nature

640(8058), 349–354 (2025) <https://doi.org/10.1038/s41586-025-08715-7>

- [31] Zemva, B., Lutar, K., Chacon, L., Fele-Beuermann, M., Allman, J., Shen, C., Bartlett, N.: Thermodynamically unstable fluorides of nickel: NiF_4 and NiF_3 syntheses and some properties. *J. Am. Chem. Soc.* **117**(40), 10025–10034 (1995) <https://doi.org/10.1021/ja00145a013>
- [32] Mattsson, S., Paulus, B.: Density functional theory calculations of structural, electronic, and magnetic properties of the 3d metal trifluorides MF_3 ($M = \text{Ti–Ni}$) in the solid state. *J. Comput. Chem.* **40**(11), 1190–1197 (2019) <https://doi.org/10.1002/jcc.25777>
- [33] Goodenough, J.B.: Goodenough-Kanamori rule. *Scholarpedia* **3**(10), 7382 (2008) <https://doi.org/10.4249/scholarpedia.7382> . revision #122456
- [34] Supplemental material
- [35] Wang, K.-L., Huang, W., Cao, Q.-H., Zhao, Y.-J., Sun, X.-J., Ding, R., Lin, W.-W., Liu, E.-H., Gao, P.: Engineering $\text{NiF}_3/\text{Ni}_2\text{P}$ heterojunction as efficient electrocatalysts for urea oxidation and splitting. *Chem. Eng. J.* **427**, 130865 (2022) <https://doi.org/10.1016/j.cej.2021.130865>
- [36] Effenberger, H., Mereiter, K., Zemann, J.: Crystal structure refinements of magnesite, calcite, rhodochrosite, siderite, smithonite, and dolomite, with discussion of some aspects of the stereochemistry of calcite type carbonates. *Z. Kristallogr. Cryst. Mater.* **156**(1-4), 233–244 (1981)
- [37] Alikhanov, R.A.: Neutron diffraction investigation of the antiferromagnetism of the carbonates of manganese and iron. *Sov. Phys. JETP-USSR* **9**(6), 1204–1208 (1959)
- [38] Hohenberg, P., Kohn, W.: Inhomogeneous electron gas. *Phys. Rev.* **136**, 864–871 (1964) <https://doi.org/10.1103/PhysRev.136.B864>
- [39] Kohn, W., Sham, L.J.: Self-consistent equations including exchange and correlation effects. *Phys. Rev.* **140**, 1133–1138 (1965) <https://doi.org/10.1103/PhysRev.140.A1133>
- [40] Kresse, G., Furthmüller, J.: Efficiency of ab-initio total energy calculations for metals and semiconductors using a plane-wave basis set. *Comput. Mater. Sci.* **6**(1), 15–50 (1996) [https://doi.org/10.1016/0927-0256\(96\)00008-0](https://doi.org/10.1016/0927-0256(96)00008-0)
- [41] Kresse, G., Hafner, J.: Ab initio molecular dynamics for liquid metals. *Phys. Rev. B* **47**, 558–561 (1993) <https://doi.org/10.1103/PhysRevB.47.558>
- [42] Kresse, G., Furthmüller, J.: Efficient iterative schemes for ab initio total-energy calculations using a plane-wave basis set. *Phys. Rev. B* **54**, 11169–11186 (1996)

<https://doi.org/10.1103/PhysRevB.54.11169>

- [43] Giannozzi, P., Barone, O., Bonfà, P., Brunato, D., Car, R., Carnimeo, I., Cavazzoni, C., Gironcoli, S., Delugas, P., Ferrarini, F., Ferretti, A., Marzari, N., Timrov, I., Urru, A., Baroni, S.: Quantum espresso toward the exascale. *J. Chem. Phys.* **152**(15), 154105 (2020) <https://doi.org/10.1063/5.0005082>
- [44] Perdew, J.P., Burke, K., Ernzerhof, M.: Generalized gradient approximation made simple. *Phys. Rev. Lett.* **77**, 3865–3868 (1996) <https://doi.org/10.1103/PhysRevLett.77.3865>
- [45] Sun, J.-W., Ruzsinszky, A., Perdew, J.P.: Strongly constrained and appropriately normed semilocal density functional. *Phys. Rev. Lett.* **115**, 036402 (2015) <https://doi.org/10.1103/PhysRevLett.115.036402>
- [46] Blöchl, P.E.: Projector augmented-wave method. *Phys. Rev. B* **50**, 17953–17979 (1994) <https://doi.org/10.1103/PhysRevB.50.17953>
- [47] Kresse, G., Joubert, D.: From ultrasoft pseudopotentials to the projector augmented-wave method. *Phys. Rev. B* **59**, 1758–1775 (1999) <https://doi.org/10.1103/PhysRevB.59.1758>
- [48] Anisimov, V.I., Zaanen, J., Andersen, O.K.: Band theory and mott insulators: Hubbard U instead of stoner I. *Phys. Rev. B* **44**, 943–954 (1991) <https://doi.org/10.1103/PhysRevB.44.943>
- [49] Liechtenstein, A.I., Anisimov, V.I., Zaanen, J.: Density-functional theory and strong interactions: Orbital ordering in mott-hubbard insulators. *Phys. Rev. B* **52**, 5467–5470 (1995) <https://doi.org/10.1103/PhysRevB.52.R5467>
- [50] Dudarev, S.L., Botton, G.A., Savrasov, S.Y., Humphreys, C.J., Sutton, A.P.: Electron-energy-loss spectra and the structural stability of nickel oxide: An LSDA + U study. *Phys. Rev. B* **57**, 1505–1509 (1998) <https://doi.org/10.1103/PhysRevB.57.1505>
- [51] Zhou, F., Cococcioni, M., Marianetti, C.A., Morgan, D., Ceder, G.: First-principles prediction of redox potentials in transition-metal compounds with LDA + U. *Phys. Rev. B* **70**, 235121 (2004) <https://doi.org/10.1103/PhysRevB.70.235121>
- [52] Krukau, A.V., Vydrov, O.A., Izmaylov, A.F., Scuseria, G.E.: Influence of the exchange screening parameter on the performance of screened hybrid functionals. *J. Chem. Phys.* **125**(22), 224106 (2006) <https://doi.org/10.1063/1.2404663>
- [53] Haule, K.: Quantum monte carlo impurity solver for cluster dynamical mean-field theory and electronic structure calculations with adjustable cluster base. *Phys. Rev. B* **75**, 155113 (2007) <https://doi.org/10.1103/PhysRevB.75.155113>

- [54] Haule, K., Yee, C.-H., Kim, K.: Dynamical mean-field theory within the full-potential methods: Electronic structure of CeIrIn₅, CeCoIn₅, and CeRhIn₅. Phys. Rev. B **81**, 195107 (2010) <https://doi.org/10.1103/PhysRevB.81.195107>
- [55] Haule, K.: Exact double counting in combining the dynamical mean field theory and the density functional theory. Phys. Rev. Lett. **115**, 196403 (2015) <https://doi.org/10.1103/PhysRevLett.115.196403>
- [56] Lee, S., Torii, S., Ishikawa, Y., Yonemura, M., Moyoshi, T., Kamiyama, T.: Weak-ferromagnetism of CoF₃ and FeF₃. Physica B Condens. Matter **551**, 94–97 (2018) <https://doi.org/10.1016/j.physb.2017.11.082>. The 11th International Conference on Neutron Scattering (ICNS 2017)

Acknowledgements

We thank Z.-X. Liu, X.-H. Kong, and C. Wang for valuable discussions. This work was financially supported by the National Key R&D Program of China (Grant No.2024YFA1408601), the National Natural Science Foundation of China (Grant No.12434009, No.12204533, No.62206299 and No.12174443) and the Beijing Natural Science Foundation (Grant No.Z200005). Computational resources have been provided by the Physical Laboratory of High Performance Computing at Renmin University of China.

Author contributions

P.-J.G. and Z.-Y.L. contributed to the ideation and design of the research; S.Q. and Z.-F. O. performed the calculations; P.-J.G. and Z.-Y.L. performed symmetry analysis, wrote and edited the paper; all authors contributed to the research discussions.

Competing interests

The authors declare no competing interests.

Correspondence

Appendix A Section title of first appendix

A.1 Magnetocrystalline anisotropy

In the relativistic case, the coupling of spin and lattice causes crystal material to change from spin group symmetry to magnetic group symmetry, and the direction of easy magnetization axis determines the magnetic group symmetry of the crystal material. For altermagnetic NiF₃, by calculating the magnetocrystalline anisotropy energy in both $x-y$ and $y-z$ planes, we find the easy magnetization axis is along 30 degrees, 150 degrees, and 270 degrees directions in the $x-y$ plane, deriving from the C_3

symmetry (Fig.A1 (a) and (b)). Furthermore, our analysis shows that altermagnetic NiF₃ has I, TC₂¹t and TM₁t symmetries. Thus, when soc is considered, the quadruple degenerate band on the $\Gamma - T$ axis will split into four non-degenerate bands. Different from NiF₃, the easy magnetization axis of FeCO₃ and CoF₃ have been confirmed by neutron scattering experiments and are along the z direction of the crystallographic unit cell [37, 56], which make the symmetry of FeCO₃ and CoF₃ being double point group D_{3d}.

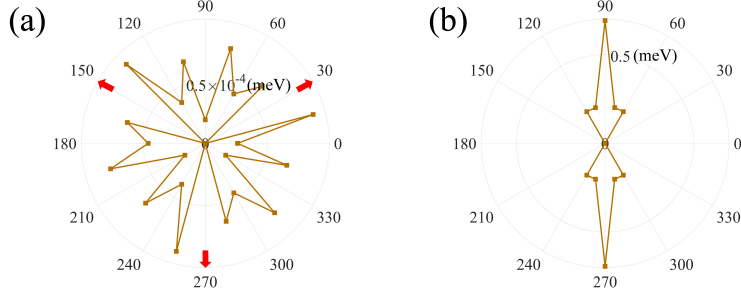


Fig. A1 Magnetocrystalline anisotropy of NiF₃ for the $x-y$ plane (a) and the $y-z$ plane (b). In (a), the x and y axes represent 0 degrees and 90 degrees, respectively. In (b), the y and z axes represent 0 degrees and 90 degrees, respectively. The red arrows represent the direction of easy magnetization axes.

A.2 The electronic structures of the other five materials

Table A1 The relationship between valence electron occupation, crystal symmetry and SOC of altermagnetic materials. The VE, QD, DD, and EO represent valence electrons, quadruple degeneracy, double degeneracy and electron occupation, respectively.

Compound	VF ₃	CrF ₃	FeF ₃	CoF ₃	NiF ₃	FeCO ₃
VE	64	66	70	72	74	72
QD	11	11	12	12	13	13
DD	10	11	11	12	12	11
EO	Full	Full	Full	Full	Half	Half
SOC	Weak	Weak	Weak	Weak	Strong	Strong

Since AF₃ (A=V, Cr, Fe, Co) and NiF₃ have the same crystal structure and magnetic structure, AF₃ (A=V, Cr, Fe, Co) are also i -wave altermagnetic materials. Different from NiF₃, the SOC effect of AF₃ is weak near the Fermi level, which are demonstrated by our calculated band structures (Fig.A2). The reason of AF₃ with weak SOC effect is that valence electrons fully occupy all bands below the Fermi level (Table. A1). Thus, these altermagnetic materials AF₃ are already semiconductors without SOC (Fig.A2).

On the other hand, the strong SOC in NiF₃ closely related to altermagnetism. To demonstrate it, we have also calculated the band structure of NiF₃ in the

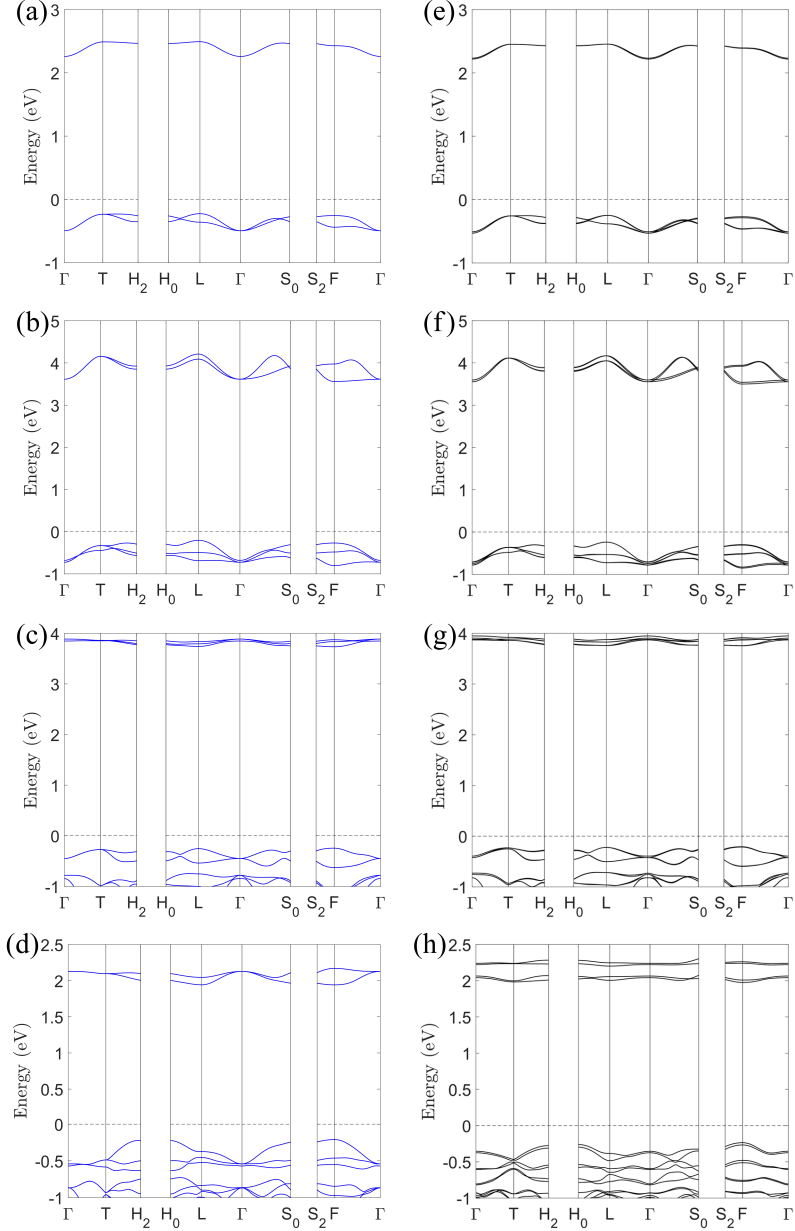


Fig. A2 The electronic band structures of AF_3 ($A=V, Cr, Fe, Co$). (a) and (e) are the electronic band structures of VF_3 without and with SOC under the correlation interaction ($U = 3.3$ eV), respectively. (b) and (f) are the electronic band structures of CrF_3 without and with SOC under the correlation interaction ($U = 3.4$ eV), respectively. (c) and (g) are the electronic band structures of FeF_3 without and with SOC under the correlation interaction ($U = 4.9$ eV), respectively. (d) and (h) are the electronic band structures of CoF_3 without and with SOC under the correlation interaction ($U = 4.0$ eV), respectively.

AFM2 antiferromagnetic state. Comparing the bands with and without SOC, AFM2 antiferromagnetic NiF_3 does not have strong SOC effect (Fig.A3 (b) and (c)).

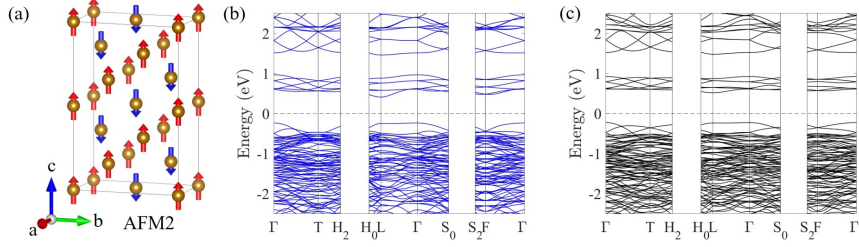


Fig. A3 (a) The magnetic structure of AFM2 for NiF_3 . The band structure along the high-symmetry direction of AFM2 NiF_3 without (b) and with (c) SOC.

The crystal structure and magnetic structure of FeCO_3 are the same as NiF_3 (Fig.A4(a) and (b)), so FeCO_3 is also an *i*-wave antiferromagnetic material (Fig.A4(c) and (e)). Interestingly, the quadruple degenerate band crossing the Fermi level is also half-filled for FeCO_3 (Fig. A4(d)). Moreover, our calculations show that the FeCO_3 also has a strong SOC effect and its SOC effect is stronger than that of NiF_3 (Fig.A4(f)). Furthermore, the orbital weight analysis shows that the quadruple degenerate band crossing the Fermi level is all contributed by $3d$ orbitals of Fe atoms (Fig.A4(d)), which is different from NiF_3 . Then, the enhanced SOC effect in FeCO_3 is deriving from symmetry and the correlation interaction. On the other hand, the magnetic structure of FeCO_3 has been confirmed by neutron scattering experiment [37], so FeCO_3 must have a strong SOC effect.

A.3 Competition between the Jahn-Teller effect and SOC effect

Table A2 The relative energies of the high and low symmetric structures of NiF_3

$U = 6.7\text{eV}$	without SOC (meV/Ni)	with SOC (meV/Ni)
High-symmetry crystal	0.00 (metal)	0.00 (insulator)
Low-symmetry crystal	-388.82 (insulator)	20.70 (insulator)

The metal state of NiF_3 is unstable without SOC. The stable insulating state of NiF_3 can be achieved through the Jahn-Teller effect or SOC effect. In order to determine which interaction dominates, we first calculate the energies of high-symmetry and low-symmetry structures without SOC, and found that low-symmetry structure is more stable than the high-symmetry structure (Table. A2). Moreover, the NiF_3 is an insulator under the low-symmetry structure. Interestingly, when SOC is considered, the stable phase changes from the low-symmetry structure to the high-symmetry structure (Table. A2). Furthermore, the low-symmetry structure can be relaxed to the

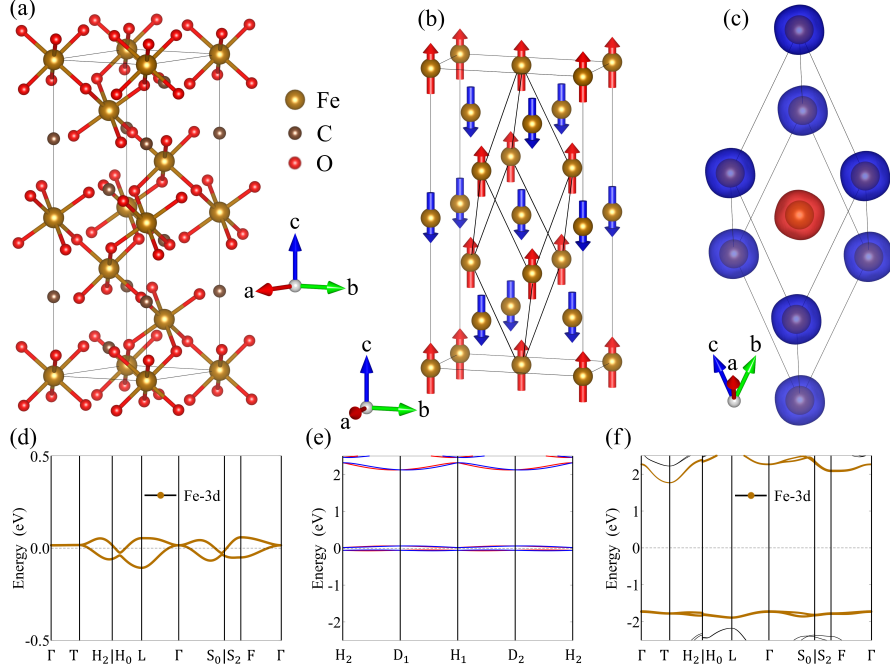


Fig. A4 The crystal structure, magnetic structure and electronic band structures of FeCO_3 . The crystal structure (a) and magnetic structure (b) where the primitive cell of FeCO_3 is given. (c) The anisotropic polarization charge densities. The red and blue represent spin-up and spin-down polarization charge density, respectively. Both (d) and (e) are the electronic band structures without SOC along the high-symmetry directions. The red and blue lines represent spin-up and spin-down bands, respectively. (f) The electronic band structure with SOC along the high-symmetry directions. The bandgap of FeCO_3 is 3.49eV under correlation interaction $U = 5\text{eV}$.

high-symmetry structure under SOC. The SOC effect dominates the electronic properties of NiF_3 rather than the Jahn-Teller effect. (The low-symmetry structure of NiF_3 is obtained by shifting the position of the F atoms.) On the other hand, in order to make our results more reliable, we calculated the electronic structures of NiF_3 without SOC by using DFT+U considered the on-site Coulomb repulsion U and Hund's coupling J , SCAN, HSE and GGA+DMFT methods, as shown in Fig.A5. From Fig.A5, NiF_3 is always metal for all methods. In addition, we also do these calculations without SOC that we set two Ni magnetic moments with different sizes and opposite directions by using GGA+U methods, which are completely consistent with those calculations in the text (Fig.2). Therefore, the conclusion that there is an extremely strong spin-orbit coupling effect in the altermagnetic NiF_3 is very reliable.

A.4 Symmetry analysis

The quadruple degenerate band of altermagnetic NiF_3 on the $\Gamma - \text{T}$ axis crossing the Fermi level is protected by spin group symmetry. According to the symmetry analysis in the text, the equivalent time-reversal spin symmetry $\{C_2^\perp T | T\}$ results in two one-dimensional irreducible complex representations of the C_3 symmetry to form

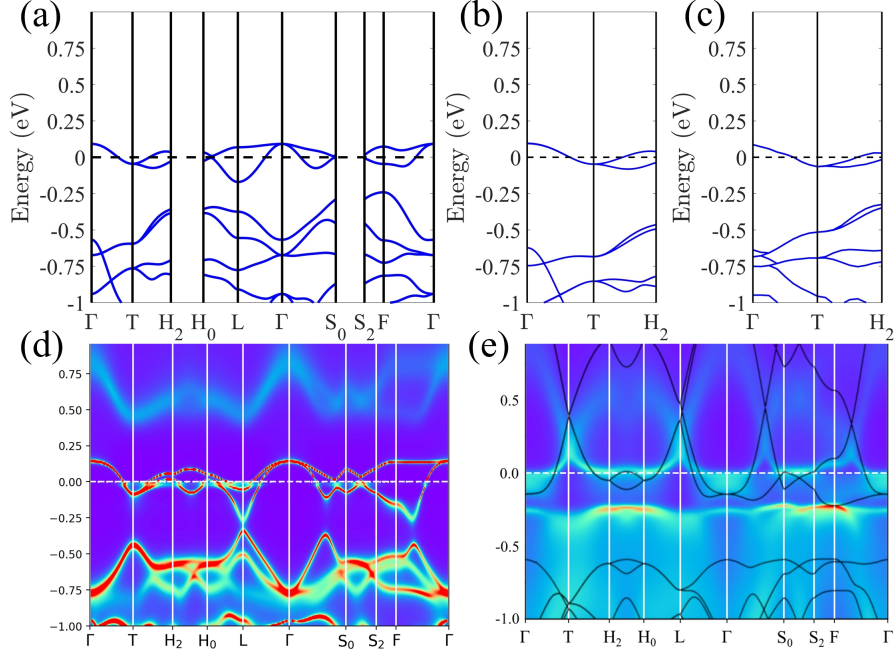


Fig. A5 The electronic band structures of altermagnetic NiF_3 without SOC by GGA+U (a), SCAN (b), HSE06 (c) and DFT+DMFT (d) methods. Momentum-resolved spectral function (e) obtained by the DFT+DMFT calculations and the black lines denote GGA+U band structure for nonmagnetic NiF_3 without SOC.

a Kramers degeneracy, and the spin symmetry $\{C_2^\perp || M_1 t\}$ protects spin degeneracy. Thus, to achieve the quadruple degenerate band on the high-symmetry axis, the crystal symmetry needs to meet two conditions: first, the high-symmetry axis has C_3 , C_4 , C_6 symmetries, and the C_3 , C_4 , C_6 symmetries can't have fractional translation; Second, the perpendicular to the high symmetry axis C_2 symmetry or the mirror symmetry M containing the high symmetry axis has fractional translation, which can connect sublattices with antiparallel spins in altermagnetic materials. By symmetry analysis, we find that there are 34 nonsymmorphic space groups satisfying these two conditions, which are shown in Table. A3. In addition, sextuple degenerate band can be also realized in altermagnetic materials with nonsymmorphic space group symmetry, for example nonsymmorphic space group $\text{Pm}\bar{3}n$.

Table A3 Altermagnetic materials with quadruple degenerate bands along the high-symmetry direction need to satisfy the crystal space group symmetry.

crystallographic system	Space group	Point group	Symmetry axis
Tetragonal	P4bm (100)	C_{4v}	C_4
Tetragonal	P4cc (103)	C_{4v}	C_4
Tetragonal	P4nc (104)	C_{4v}	C_4
Tetragonal	I4cm (108)	C_{4v}	C_4
Tetragonal	P4/mcc (124)	D_{4h}	C_4
Tetragonal	P4/mbm (127)	D_{4h}	C_4
Tetragonal	P4/mnc (128)	D_{4h}	C_4
Tetragonal	I4/mcm (140)	D_{4h}	C_4
Trigonal	P3c1 (158)	C_{3v}	C_3
Trigonal	P31c (159)	C_{3v}	C_3
Trigonal	R3c (161)	C_{3v}	C_3
Trigonal	$\bar{P}31c$ (163)	D_{3d}	C_3
Trigonal	$\bar{P}3c1$ (165)	D_{3d}	C_3
Trigonal	R3c (167)	D_{3d}	C_3
Hexagonal	P6 ₃ 22 (182)	D_6	C_6
Hexagonal	P6cc (184)	C_{6v}	C_6
Hexagonal	P6 ₃ cm (185)	C_{6v}	C_6
Hexagonal	P6 ₃ mc (186)	C_{6v}	C_6
Hexagonal	P6/mcc (192)	D_{6h}	C_6
Hexagonal	P6 ₃ /mcm (193)	D_{6h}	C_6
Hexagonal	P6 ₃ /mmc (194)	D_{6h}	C_6
Cubic	P4 ₂ 32 (208)	O	C_3
Cubic	F4 ₁ 32 (210)	O	C_3
Cubic	P4 ₃ 32 (212)	O	C_3
Cubic	P4 ₁ 32 (213)	O	C_3
Cubic	I4 ₁ 32 (214)	O	C_3
Cubic	$\bar{P}43n$ (218)	T_d	C_3
Cubic	F43c (219)	T_d	C_3
Cubic	I43d (220)	T_d	C_3
Cubic	Pm3n (223)	O_h	C_3
Cubic	Fm3c (226)	O_h	C_3
Cubic	Fd3m (227)	O_h	C_3
Cubic	Fd3c (228)	O_h	C_3
Cubic	Ia3d (230)	O_h	C_3